Journal of Materials Chemistry A

ROYAL SOCIETY OF CHEMISTRY

PAPER

View Article Online
View Journal

Cite this: DOI: 10.1039/d2ta07197e

Giant spin-dependent Seebeck effect from fully spin-polarized carriers in n-doped $EuTiO_3$: a prototype material for spin-caloritronic applications†

P. Wadhwa, [a] A. Bosin [a] and A. Filippetti *[ab]

Received 13th September 2022
Accepted 5th December 2022

DOI: 10.1039/d2ta07197e

rsc.li/materials-a

Spin-caloritronics, the generation of spin currents and spin voltages from an applied temperature gradient, is a visionary technology with outstanding potential for novel applications and a fascinating landscape of fundamental properties. These capabilities have been revealed so far in a variety of devices typically assembled as interfaces between magnetic and non-magnetic materials. Here, using advanced *ab initio* calculations, we provide evidence that giant effects can be obtained in the electron-doped bulk oxide $EuTiO_3$. We find this material to be a half-metal, 100% spin-polarized ferromagnet for a wide range of temperatures and carrier concentrations. The combination of high electron mobility, a large Seebeck coefficient, and full spin polarization realizes the perfect conditions to achieve giant spin-polarized thermopower and huge chemical potential imbalance between the spin channels. At low temperatures, our calculations predict spin current densities $\sim$0.1 mA cm^{-2} per unitary temperature gradient, and spin voltages of mV K^{-1} order, which are among the highest reported so far. In addition, our analysis lays down fundamental guidelines for the design of the best suited materials for spin-caloritronic applications.

1. Introduction

Thermoelectric materials furnish, through the Seebeck effect, the cleanest and most straightforward method to produce electrical power from heating or, *vice versa*, heating and cooling from an electric source. Alas, practical uses have been mostly limited, so far, to high-temperature applications, due to a room-T efficiency which is typically too low to compete with other energy sources. However, in 2008 an exciting new avenue opened for thermoelectricity: measurements on a device made of a ferromagnetic metallic (FM) layer of $Ni_{81}Fe_{19}$ interfaced with a non-magnetic metal (NM) showed for the first time[1] that it is possible to convert an applied temperature gradient not only into a charge current, but also into a spin current, to be eventually exploited as an information or energy carrier. This landmark result represented the coming together of two worlds, until then considered distinct: thermoelectricity and spintronics. Since then, a new research area, named spin-caloritronics, has flourished at a fast pace, driven by a series of enthralling results showing that magneto-thermal conversion can be achieved using ferromagnetic metals,[1,2] semiconductors,[3,4] insulators,[5] magnetic tunnel junctions,[6] FM/NM/FM spin valves,[7,8] and even non-magnetic materials.[9] More recently it was revealed that spin-caloritronic effects can be also derived by nuclear spins.[10] These studies on the one hand had the merit to shed light on unexplored phenomena concerning the thermal behaviour of the matter.[11,12] On the other, they implemented a variety of magnetothermal devices capable of generating, manipulating and controlling spin, charge, and heat currents.[13–17] Most of these devices are made out of an interface between a magnetic and a non-magnetic material: in the former, a spin current is generated by magnetothermal conversion and then injected in the non-magnetic side, where the current can be converted into a voltage by *e.g.* spin-Hall or Rashba–Edelstein effects. Theoretical analysis revealed that two distinct mechanisms can drive the thermal-spin current conversion: one is based on carrier diffusion which is only present in metals and semiconductors; the other is driven by magnons, *i.e.* thermally induced spin excitations which can give rise to a spin current even in insulators. To distinguish them, in the literature they are conventionally referred to as the spin-polarized Seebeck effect (SPSE), and the spin-Seebeck effect (SSE), respectively.[17] In this work we will specifically focus on the SPSE in magnetic semiconductors. Also, to avoid confusion among the many magnetothermal phenomena described in the literature, we should keep in mind that SPSE and SSE are longitudinal effects, thus conceptually well distinguished from

[a]*Dipartimento di Fisica, Università di Cagliari, S.P. Monserrato Sestu Km.0,700, Monserrato, Ca 09042-I, Italy*

[b]*Consiglio Nazionale delle Ricerche, Istituto Officina dei Materiali, CNR-IOM, S.P. Monserrato Sestu Km.0,700, Monserrato, Ca 09042-I, Italy. E-mail: alessio.filippetti@dsf.unica.it*

† Electronic supplementary information (ESI) available. See DOI: https://doi.org/10.1039/d2ta07197e

the Hall-type transverse effects which often occur simultaneously to the longitudinal ones.

In the SPSE, the spin signal propagates along with charge carriers. A robust and long-lasting spin current requires robust magnetization and a spin-diffusion length clearly longer than the sample size through which the signal propagates. These characteristics are often in contrast, since magnetization is typically carried out by rather localized, poorly mobile carriers, such as those present at the band edges of transition metal compounds. According to the Elliot–Yafet model[18–20] which rules spin scattering in centrosymmetric metals and semiconductors, spin-flip and electron scattering rates are proportional to each other,[21] thus a small mobility is reflected in small spin relaxation times. Here, using a combination of advanced *ab initio* calculations and models based on Bloch–Boltzmann Theory (BBT), we give evidence that electron-doped $EuTiO_3$ (ETO) represents a very promising material for the implementation of a giant SPSE. In fact, we will see that the additional electron charge populates almost exclusively the highly mobile Ti 3d conduction bands which, in addition, are ~100% spin-polarized at low temperatures due to the strong orbital coupling with Eu 4f magnetic moments. Thus, an optimal scenario can be envisaged, where fully spin-polarized yet itinerant electrons give rise to giant spin-polarized thermopower, and in turn spin current and spin voltage accumulation at the edges of the sample where the temperature gradient is applied.

2. Theory and methods

Spin-polarized thermoelectric transport

In the presence of electric and temperature fields, the electronic current reads, to linear order:

$$J_i = -\sigma_{ij}(\mathsf{E}_j + S_{jk}\nabla_k T) \tag{1}$$

where σ and S are conductivity and thermopower (*i.e.* Seebeck coefficient) at zero electric and temperature field, respectively. For a ferromagnetic metal, assuming fixed magnetization axis and discardable spin–orbit coupling, the current can be separated in up-spin (say majority) and down-spin (minority) independent channels. In closed circuit conditions and in absence of electric field, the currents for the two spin channels are (we get rid of cartesian indices assuming purely longitudinal response):

$$J^{\uparrow} = -\sigma^{\uparrow}S^{\uparrow}\nabla T,\ J^{\downarrow} = -\sigma^{\downarrow}S^{\downarrow}\nabla T \tag{2}$$

In general, for a ferromagnet the two channels will have different conductivities and Seebeck coefficients, and then different spin-dependent currents. We define a spin current density as the difference of up-spin and down-spin current densities:

$$J_s = J^{\uparrow} - J^{\downarrow} = -\left(\frac{\sigma^{\uparrow}}{\sigma}S^{\uparrow} - \frac{\sigma^{\downarrow}}{\sigma}S^{\downarrow}\right)\sigma\nabla T \tag{3}$$

More significant in terms of thermoelectric performance is the spin current density generated by a unitary temperature gradient:

$$\frac{J_s}{\nabla T} = \sigma^{\downarrow}S^{\downarrow} - \sigma^{\uparrow}S^{\uparrow} \tag{4}$$

Under open circuit conditions ($J^{\uparrow,\downarrow} = 0$), from eqn (1) we have:

$$S^{\uparrow,\downarrow} = -\frac{E^{\uparrow,\downarrow}}{\nabla T} = -\frac{\mathrm{d}V^{\uparrow,\downarrow}}{\mathrm{d}T} \tag{5}$$

From which S can be understood as the electromotive force generated along the gradient direction by a unitary temperature change. A spin-dependent Seebeck coefficient thus results in a spin-dependent voltage. This condition is illustrated in Fig. 1: a temperature gradient ΔT (indicated by the color bar) is applied between the ends of the sample. Specifically, we assume the center of the bar at the equilibrium temperature, and a change of temperature $\Delta T/2$ applied on each end. The temperature gradient pushes both majority and minority electrons to diffuse from the hotter to the colder side, thus generating, under open circuit conditions, electron chemical potential gradients $\nabla\mu^{\uparrow,\downarrow}$ between the two ends, with more electrons and higher chemical potential $\mu^{\uparrow,\downarrow}$ (with respect to the equilibrium state) on the colder side, and less electrons and lower $\mu^{\uparrow,\downarrow}$ on the hotter side. It is clear then that $\nabla\mu^{\uparrow,\downarrow}$ are negative in the direction of increasing temperature. If the temperature changes linearly along the bar, also $\mu^{\uparrow,\downarrow}$ change linearly, intersecting the equilibrium Fermi energy ε_F at the bar center. Chemical potentials,

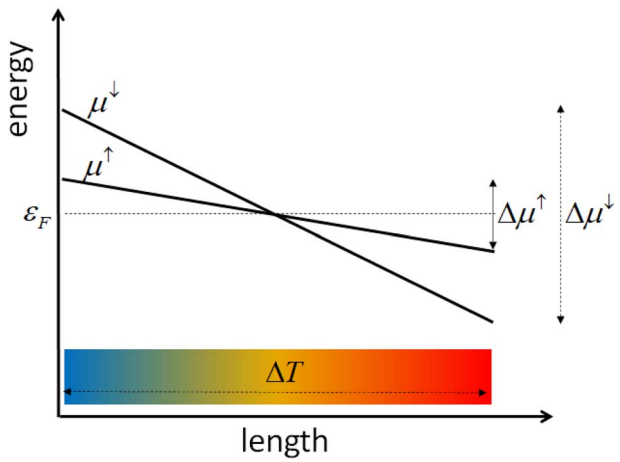

Fig. 1 Sketch of majority (up-spin) and minority (down-spin) electron chemical potential profiles along the sample, generated by the temperature gradient ΔT. At the equilibrium temperature (middle point of the sample) they match the Fermi energy; when ΔT is applied, carriers diffuse from the hot (red) to the cold (blue) side in both majority and minority channels. Due to the large spin-polarization and the different population of the two channels, the same temperature gradient generates different potential build up in the two channels, and as a consequence, different chemical potentials at each end of the sample (see text).

voltage gradients, and Seebeck coefficients for the electrons are related by the relationships:

$$\nabla\mu^{\uparrow,\downarrow} = -e\nabla V^{\uparrow,\downarrow} = eS^{\uparrow,\downarrow}\nabla T \quad (6)$$

This shows that the Seebeck coefficient is negative for electrons. It is important to note that in Fig. 1 we draw $\nabla\mu^{\uparrow,\downarrow}$ larger in magnitude for the minority carriers, *i.e.* for the less populated bands. This can be understood considering that the voltage generated by the temperature gradient corresponds to the work necessary to move a single electron across the bar. For this work, an activation energy $\varepsilon_F - \varepsilon_{CBB}^{\uparrow,\downarrow}$ is required, where $\varepsilon_{CBB}^{\uparrow,\downarrow}$ are the conduction band bottom energies of the two spin channels. In fact, at low or moderate doping, it is well known that $S^{\uparrow,\downarrow} \sim (\varepsilon_F - \varepsilon_{CBB}^{\uparrow,\downarrow})/eT$, and thus $|S^{\downarrow}| > |S^{\uparrow}|$. On the other hand, under closed circuit conditions $J^{\uparrow} \gg J^{\downarrow}$ (see eqn (2)) since conductivity is typically much larger for majority carriers. A specific case will be described in the results section.

From Fig. 1, we see that the difference in up-spin and down-spin potential gradients generates a difference between up-spin and down-spin chemical potentials at the two ends of the sample:

$$\mu^{\uparrow} - \mu^{\downarrow} = \pm\frac{1}{2}\Delta\left(\mu^{\uparrow} - \mu^{\downarrow}\right) = \pm e\left(S^{\uparrow} - S^{\downarrow}\right)\frac{\Delta T}{2} = eV_s \quad (7)$$

where the upper and lower signs are for the hotter and colder ends, respectively. This difference defines the spin voltage V_s which, together with the spin current J_s, is the essential signature of the SPSE or SSE, and the primary subject of interest of this work. The spin voltage generated by a unitary temperature interval is:

$$\frac{V_s}{\Delta T} = \pm\frac{S^{\uparrow} - S^{\downarrow}}{2} \quad (8)$$

Since we assumed $|S^{\downarrow}| > |S^{\uparrow}|$, it follows from eqn (7) and (8) that V_s is positive at the colder end, and negative at the hotter end.

The Bloch–Boltzmann approach

Conductivity and the Seebeck coefficient are calculated according to Bloch–Boltzmann Theory (BBT),[22,23] which combines Boltzmann theory for the electronic transport with *ab initio* band energies. Our approach was successfully applied in the past to a wide variety of materials.[24–29] Here we briefly recall the main formulae, while the detailed formulation can be found in ref. [28] and 29. For simplicity, we drop cartesian indices assuming purely longitudinal transport. For a multiband ferromagnetic system, total conductivity and the Seebeck coefficient are:*i.e.*

$$\sigma = \sigma^{\uparrow} + \sigma^{\downarrow} = \sum_{n\uparrow}\sigma_n^{\uparrow} + \sum_{n\downarrow}\sigma_n^{\downarrow} \quad (9)$$

$$S = \frac{\sigma^{\uparrow}S^{\uparrow}}{\sigma} + \frac{\sigma^{\downarrow}S^{\downarrow}}{\sigma} = \sum_{n\uparrow}\frac{\sigma_n^{\uparrow}S_n^{\uparrow}}{\sigma} + \sum_{n\downarrow}\frac{\sigma_n^{\downarrow}S_n^{\downarrow}}{\sigma} \quad (10)$$

the total Seebeck coefficient is the sum of spin-dependent components, weighted over the relative spin conductivity. From eqn (9) and (10) we derive the definition of spin-dependent Seebeck coefficients:

$$S^{\uparrow,\downarrow} = \sum_{n\uparrow,\downarrow}\frac{\sigma_n^{\uparrow,\downarrow}S_n^{\uparrow,\downarrow}}{\sigma^{\uparrow,\downarrow}} \quad (11)$$

where band conductivity and the band Seebeck coefficient are, in BBT:HH

$$\sigma_n^{\uparrow,\downarrow} = \left(\frac{e^2}{V}\right)\int \mathrm{d}k\; g(k)\tau_{nk}^{\uparrow,\downarrow}\left(-\frac{\partial f}{\partial\varepsilon_{nk}^{\uparrow,\downarrow}}\right)\left(v_{nk}^{\uparrow,\downarrow}\right)^2 \quad (12)$$

$$S_n^{\uparrow,\downarrow} = -\left(\frac{e}{VT\sigma_n^{\uparrow,\downarrow}}\right)\int \mathrm{d}k\; g(k)\tau_{nk}^{\uparrow,\downarrow}\left(\varepsilon_{nk}^{\uparrow,\downarrow} - \varepsilon_F\right)\left(-\frac{\partial f}{\partial\varepsilon_{nk}^{\uparrow,\downarrow}}\right)\left(v_{nk}^{\uparrow,\downarrow}\right)^2 \quad (13)$$

ere V is the sample volume, f the Fermi occupancy, ε_{nk} and v_{nk} are band energies and velocities, g is the density of states, and τ_{nk} is the electronic relaxation time. The integrals over the Brillouin Zone (BZ) are calculated by k-space interpolation of *ab initio* band energies, while τ_{nk} is determined by numerical models[28] which include electron scattering with impurities, acoustic phonons, and polar optical phonons. Finally, we assume the spin-flip scattering discardable with respect to the electron scattering, *i.e.* spin relaxation time τ_s is much longer than τ_{nk}. In our case of interest (Ti 3d conduction bands in oxides) this is largely justified since $\tau_{nk} \sim 10$ fs and spin–orbit coupling is small (∼meV); thus we can expect τ_s no less than one or two orders of magnitude longer.

Ab initio band structure calculations

Theoretical calculations are performed within the framework of Density Functional Theory (DFT) as implemented in the VASP code.[30] Wavefunctions are expressed according to the projected augmented wave (PAW) method[31] with an energy cut-off of 550 eV; Generalized Gradient Approximation (GGA)[32] is used to describe the exchange–correlation energy. For sampling the BZ, up to 20 × 20 × 20 Monkhorst–Pack mesh is used. The atomic positions are fully relaxed up to a force threshold on each atom of 1 meV Å^{-1}. Finally, in order to overcome the well known DFT inaccuracy in the description of strongly correlated systems, GGA + U[33] is used for all the reported properties. While generally not as accurate as hybrid or self-interaction corrected functionals in the description of 4f states,[34,35] we found that GGA + U is still adequate to describe the properties of interest in this work. We assume U = 7.5 eV and 4.0 eV for Eu 4f and Ti 3d states, respectively: previous studies showed that these values deliver a calculated band structure for ETO in nice agreement with photoemission measurements.[36,37]

3. Results

Overview of the ETO properties

ETO is rich in peculiar characteristics which make this material one of the most investigated oxides in the last 15 years or so. Ironically, while this material in the pristine undoped phase is neither ferroelectric nor ferromagnetic, it is characterized by

remarkably strong coupling between structural, electric, and magnetic properties.[38–45] At room-*T*, it is a cubic semiconductor, with band gap ~1 eV and lattice parameter $a = 3.905$ Å, virtually identical to those of $SrTiO_3$ (STO). The structural similarity makes ETO perfectly suited to be epitaxially grown on STO substrates and integrable in oxide heterostructures.[37,46–49] Unlike STO, ETO features a large intrinsic magnetization embodied in the fully spin-polarized Eu 4f states; Owing to the strong 4f orbital localization, the pristine material is a paramagnetic semiconductor at room-*T*, and becomes antiferromagnetic (AFM) below $T_N = 5.2$ K; this long-range order is imputed to the Eu 4f–Ti 3d orbital coupling, as described by a number of experimental and theoretical investigations.[50–53] Also similarly to STO, ETO displays huge electric permittivity (~160 at room-*T*), which undergoes large changes upon application of a magnetic field.[38] Strong magnetocapacitance and magnetostriction[42,43] can be traced back to the magnetic field-induced softening of the IR-active TO1 polar mode, which governs permittivity at room-*T*.[54–57] Lattice coupling to electronic and magnetic properties was further proved by discovering that application of ~1% tensile strain can make this material multiferroic, *i.e.* simultaneously ferroelectric and ferromagnetic.[40,50] No less spectacular is the magnetotransport behavior: a number of experiments coherently show that n-doping is effective in inducing a FM phase transition. This can be achieved by A-site doping ($Eu_{1-x}La_xTiO_3$),[50,58] B-site doping ($EuTi_{1-x}Nb_xO_3$),[59,60] and even O-doping ($EuTiO_{3-x}H_x$).[61] Coherently with this scenario, the 2DEG spontaneously formed at the STO/ETO/LAO interface[62–65] is also reported to order ferromagnetically. The spin-polarized carriers in ETO are found to generate a number of intriguing magnetotransport phenomena, including anisotropic magnetoresistance,[66,67] the anomalous

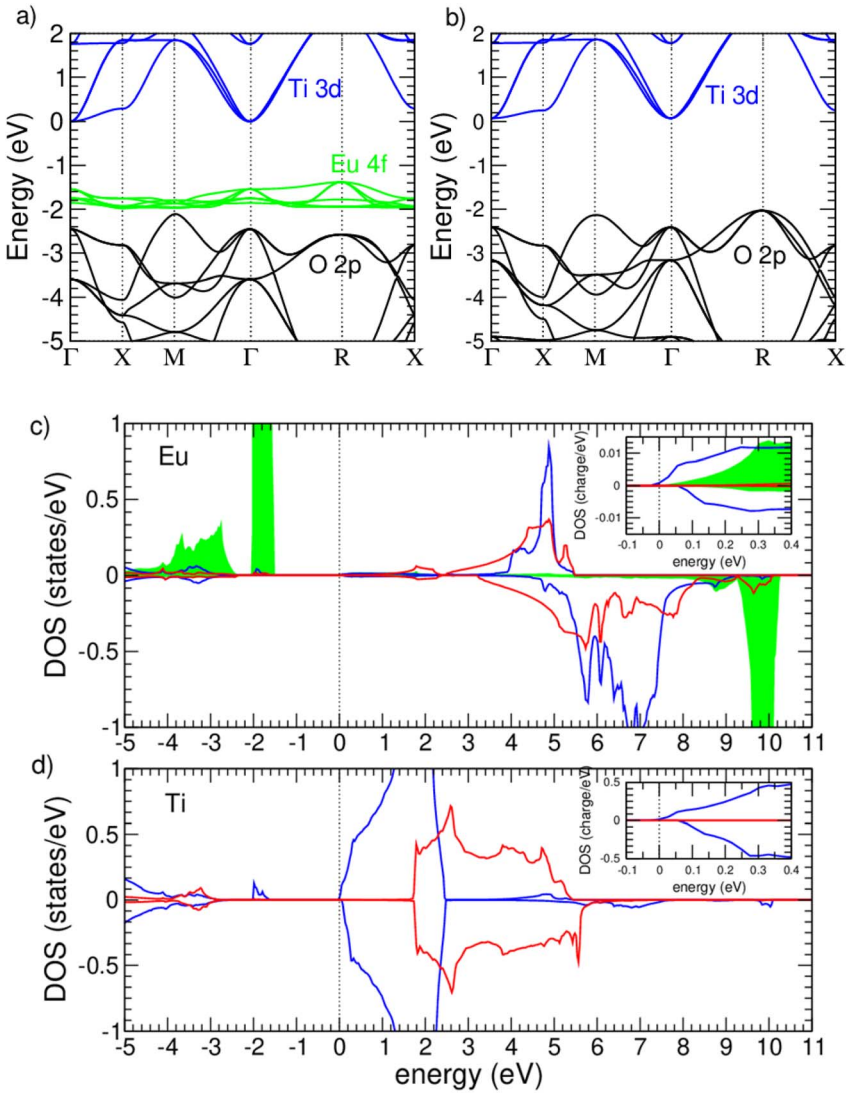

Fig. 2 Electronic properties of FM ETO calculated using GGA + *U*. (a and b) Band energies for majority (up-spin) and minority (down-spin) components, respectively. The prevailing orbital character is indicated by label. (c) Orbital-resolved density of states for Eu. Positive and negative curves are for up-spin and down-spin components, respectively. Green, blue, and red correspond to the contribution of 4f, t_{2g}, and e_g orbitals, respectively. Insets show an enlarged view around the CBB. (d) Orbital-resolved DOS for Ti. Labels are the same as in (c).

Hall effect,[68–70] and the giant magnetocaloric effect.[71] In what follows we first discuss the properties of undoped ETO, and then the effect of electron doping.

Undoped ETO

Pristine bulk ETO at room-T has a cubic $Pm3m$ perovskite crystal structure, with G-type AFM order, as indicated by neutron diffraction studies. However, the AFM *vs.* FM competition is extremely tight, as a consequence of exchange interactions of ∼meV order, whose sign can be reverted by strain[51] or charge injection.[58] Since n-doped ETO is our primary subject of interest, hereafter our results will mainly focus on the FM phase. Also, we discard the $Pm3m$ to $I4/mcm$ structural transition observed at 235 K,[48,72,73] characterized by $(a^0a^0c^-)$ octahedral tilting ∼3° and $a/c \sim 0.998$, as they are too tiny distortions to give any visible effect on our results.

In Fig. 2 the band structure and orbital-resolved density of states calculated using GGA + U for the FM phase are shown. The gap region displays three well distinct band groups: the Ti 3d t_{2g} states at the conduction band bottom (CBB), the fully spin-polarized Eu 4f states with a nominal magnetization of 7 μ_B/Eu at the valence band top (VBT), and the O 2p states which mainly contribute to the valence bands. We obtain an indirect band gap of 1.51 eV between the Eu 4f VBT at the R point and the Ti 3d CBB at the Γ point, slightly larger than the direct band gap at Γ. We found the centroid of the Eu 4f states located at a bonding energy ∼1.8 eV, in good agreement with the 2 eV peak found by ARPES[37] and XPS.[52]

In experiments, the 4f peak displays a ∼2 eV spectral width which is much larger than the calculated ∼0.5 eV bandwidth. This discrepancy, clearly due to the electron–phonon coupling contribution absent in the band calculation, causes the 30% overestimation of our band gap with respect to the observed absorption threshold of 0.96 eV.[52]

From the calculated DOS, we obtain a large 4f spin-splitting ∼11 eV, due to the strong Coulomb repulsion at half-filling. A long-debated question concerns the fundamental mechanism withwhich these big, spatially localized magnetic moments give rise to long-range magnetic order.[51,58] Two elements are invoked to the aim: the direct Eu 4f–Ti t_{2g} superexchange coupling, allegedly leading to the observed AFM order, and an indirect ferromagnetic exchange, mediated by virtual Eu 4f–5d t_{2g} intra-atomic excitations and Eu 5d t_{2g}–Ti 3d t_{2g} coupling. In fact, our calculated DOS indicates that both mechanisms are in action: the enlargement around the CBB (Fig. 2d, inset) shows that the Ti t_{2g} band manifold is spin-split; furthermore, in this small scale we can see (Fig. 2c, inset) the presence of magnetically split Eu 4f and 5d t_{2g} orbitals at the CBB as well. Strong proximity effects mediated by these two orbital channels can then inject spin-polarization into the conduction bands. The intra-atomic Eu 4f–5d spin coupling is apparent from the Eu DOS: albeit empty, the 5d t_{2g} DOS peak displays a large 2 eV splitting. The 5d e_g DOS is also visibly split, but it is less important than the Eu 5d t_{2g}–Ti 3d t_{2g} overlap. Consistent with this picture, we obtain magnetic moments of ∼6.95 μ_B, ∼0.05 μ_B, and ∼0.01 μ_B for Eu 4f, Eu 5d, and Ti 3d states, respectively. Most importantly, the Ti t_{2g} bands display a large exchange splitting of ∼70 meV at the band bottom. Interestingly we see that Eu 5d states have inverted crystal splitting, *i.e.* e_g states lower than t_{2g}. This happens because for Eu the t_{2g} are the orbitals pointing towards oxygens, so they are electrostatically more repelled than e_g's.

A crucial feature of our analysis concerns the chemical nature of Eu 5d orbitals. Unlike 3d, 5d orbitals are spread in a wide space region, and substantially overlap with the surrounding Eu 4f, Ti 3d, and O p states. This has two important consequences: first, they efficiently act as connecting bridges between Eu and Ti states, thus favoring long-range magnetic coupling, as described above. Second, they favor a bigger bandwidth and higher electron mobility than in 3d-only titanates. Consistently, we obtain CBB effective masses of $0.39m_e$ and $5.64m_e$ for the t_{2g} planar doublet and the orthogonal singlet, respectively. These values are remarkably smaller than the corresponding $\sim 0.7m_e$ and $\sim 8m_e$ for STO.

Electron doping

In this section we simulate the introduction of electron charge by explicitly adding electrons to the system, without actual atomic substitutions. This method is largely used in *ab initio* calculations to mimic experimental situations where charging is not accompanied by strong structural disorder or by localization effects which dramatically alter the electronic properties around the band gap, as in the case of field effect modulation or shallow point defects. The same approach was previously applied in ref. [58], where a detailed map of the exchange-interaction parameters is obtained as a function of carrier concentration. Here we focus on a different aspect: the conduction band evolution and the progressive spin splitting at varying electron charges.

In Fig. 3a we display the calculated nearest-neighbor exchange-interaction parameter extracted from a Heisenberg Hamiltonian $H = -J\sum_{ij} S_i \times S_j$ as a function of the electron charge ranging from $q = 0$ to $q = 0.2$ electrons per f.u., corresponding to a carrier concentration $n = 3.2 \times 10^{21}$ cm^{-3}; here a positive J means FM phase stability. We can see that the additional electron charge dramatically enhances the FM stability. This enhancement occurs even for the lattice parameter fixed at the experimental value (blue dots); when leaving the lattice parameter to relax (red dots), the FM phase stability strengthens even further. The reason can be understood from Fig. 3b: additional electrons generate an almost linear increase of lattice parameter; this volume expansion favors the FM phase, as explained in detail in ref. [51]. Thus, the additional charge causes two separate effects, both favoring the FM order: a lattice-frozen, purely electronic orbital filling, and a progressive lattice expansion. Notice also that the FM phase is already stable at zero doping, at odds with the observations. In fact, a crude mean-field experimental estimate for undoped ETO gives $J = -0.15$ meV; as is well known, *ab initio* methods struggle in predicting exchange-interactions of such a tiny amplitude. Experimentally, the FM phase is found to set in for x

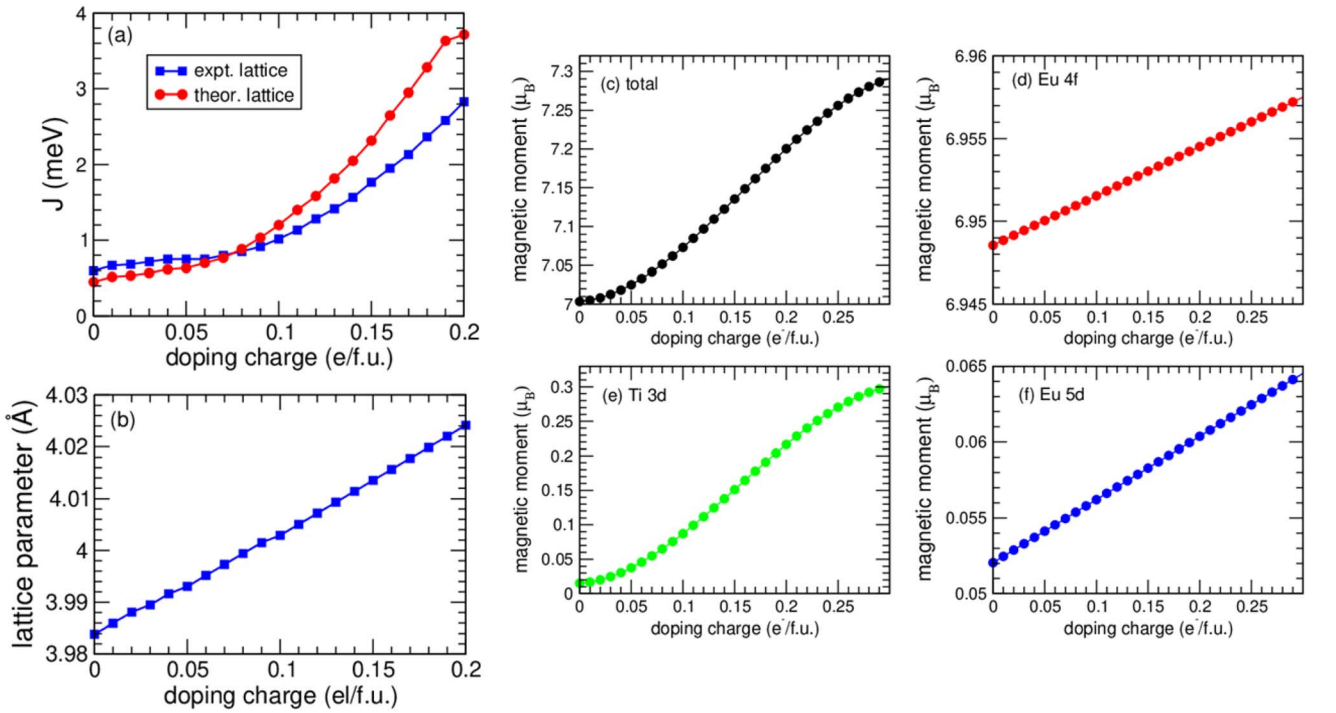

Fig. 3 (a) Exchange-interaction parameter of bulk ETO at varying electron charges q, calculated using GGA + U. Blue points are obtained for the lattice parameter kept fixed at the experimental value; red points are after structural relaxation. (b) Optimized lattice parameter. (c) Total magnetization per f.u. (d, e and (f) Magnetic moment contributions coming from Eu 4f, Ti 3d, and Eu 5d states, respectively.

> 0.1 in $Eu_{1-x}La_xTiO_3$ (ref. 50) with $T_c = 8$ K, and for $x > 0.05$ in $EuTi_{1-x}Nb_xO_3$,[59] with $T_c \sim 9$ K.

In Fig. 3c the magnetization evolution with charge is shown. Remarkably, magnetization increases almost as a straight line, *i.e.* all the electron charges contribute to it. Specifically, most of the charge fills the Ti 3d magnetic moments, but tiny increments are also found for the magnetic moments of Eu 4f and 5d states. These residual values are a clear manifestation of the Eu 4f–Ti 3d and Eu 5d–Ti 3d overlaps discussed in the previous section.

In Fig. 4 majority and minority band energies for the FM phase are plot in a small region around the CBB, for specific charge content. We see that a remarkable CBB spin-splitting $\Delta\varepsilon_{CBB} = \varepsilon^{\downarrow}_{CBB} - \varepsilon^{\uparrow}_{CBB}$ is present even for the undoped case; the splitting is progressively enhanced by the increase of charge content in the conduction bands. This behavior can be approximatively rationalized in terms of a simple linear extrapolation:

$$\Delta\varepsilon_{CBB} = J_{3d} + qU_{3d} \quad (14)$$

where $J_{3d} = 69$ meV is an interatomic exchange-interaction, and $U_{3d} \sim 5$ eV is the t_{2g} on-site Coulomb repulsion.

It is important noting that the large U_{3d} value causes a fast increment of $\Delta\varepsilon_{CBB}$ with q, and in turn, a fast rise of the spin-polarized charge fraction, as shown by the $T = 0$ Fermi level position in Fig. 4. In the following sections, we will provide evidence that, in a wide charge density and temperature range, n-doped FM ETO behaves as a fully spin-polarized material, as recently confirmed by Shubnikov–de Haas experiments.[67] These findings depict an ideal scenario where a giant SPSE can be envisaged.

Electric and thermoelectric transport

Band structure calculation results at varying doping charges are used as input in eqn (12) and (13) for the determination of conductivity and the Seebeck coefficient *vs.* T. We point out that in our data T dependence is included in band occupancy and in electron scattering, but not in the electronic structure, nominally fixed at $T = 0$. The electronic relaxation time is determined by models which require input parameters related to the electron–phonon and electron-impurity scattering. At room T, for polar materials, electron scattering with LO phonons is by far and large the dominant mobility-limiting process.[74] The key parameter which sets the LO coupling strength is the Frölich prefactor $\sqrt{m^*}(\varepsilon_\infty{}^{-1} - \varepsilon_0{}^{-1})$;[75,76] a huge difference between ε_∞ and ε_0 (IR measurements for ETO[57] at room T give 5.88 and 160, respectively) is the signature of a highly polar, insulating character. The temperature dependence is set by the three LO phonon energies; extrapolating from plasma frequency measurements (details are given in the SI) we obtain $\omega_{LO,1} = 19$ meV, $\omega_{LO,2} = 60$ meV, and $\omega_{LO,3} = 92$ meV. At low-T, for clean or weakly doped samples, mobility is governed by scattering with acoustic phonons. Within linear dispersion approximation, this process can be modelled according to two key parameters: the deformation potential ($D = 3.74$ eV, calculated from our band

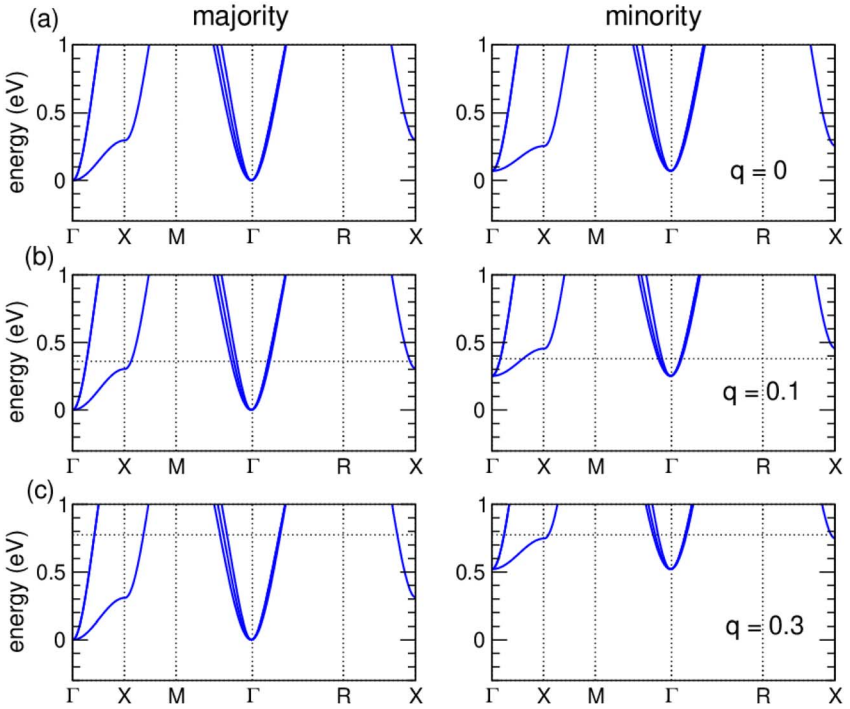

Fig. 4 Band structure of spin majority and spin minority carriers for the FM ETO bulk. (a) No doping ($q = 0$), (b) $q = 0.1$ el per f.u. doping, (c) $q = 0.3$ el per f.u. doping; zero energy is fixed at the CBB of the majority carriers, corresponding to the absolute CBB. The dotted horizontal lines indicate the Fermi level at zero temperature.

structure) and the sound velocity *vs.* $= 1.5 \times 10^5$ cm s^{-1}.[30] Finally, electron-impurity scattering, which becomes important at low T for heavily doped samples, is described according to the classical Brooks–Herring formula.[30]

In Fig. 5a, we display the calculated mobility for the n-doped FM ETO phase at several carrier concentrations; the mobility for the G-type AF phase (not shown) is rather similar and only about 10% lower due to the slightly smaller bandwidth of the AF phase. In Fig. 5b we display again the electron mobility for FM ETO but now excluding the contribution from impurity scattering, which is more appropriate to describe field effect charge modulation or weakly doped samples. In the absence of

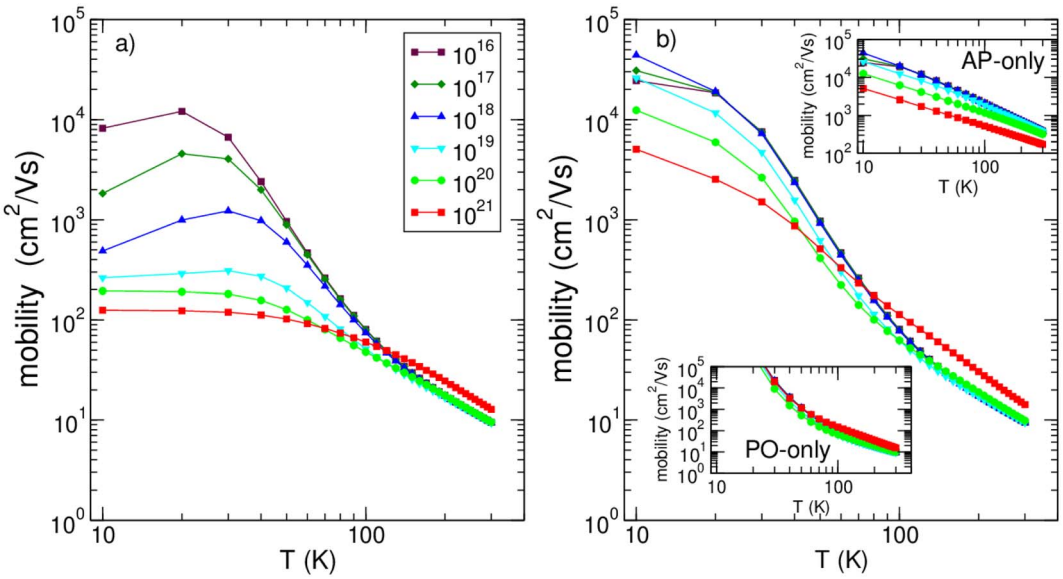

Fig. 5 Calculated mobility *vs.* T for FM ETO; curves of different colors correspond to different charge concentrations, indicated in the legend in el per cm^3 unit. (a) Electron mobility determined including all the scattering processes (see text); (b) mobility including all the scattering sources except electron-impurity scattering. Insets: mobilities determined exclusively from acoustic phonon scattering (AP-only) which govern low-T, and polar optical phonon scattering (PO-only) which rules the room-T behavior. Labels are the same as in (a).

significant impurity concentration, we obtain large mobility $\sim 10^4$ cm^2 V^{-1} s^{-1} at low-T, and ~ 10 cm^2 V^{-1} s^{-1} around room-T. These results are validated by the nice agreement with transport measurements.[50,67,68] In the insets of Fig. 5c, we also show acoustic phonon-only and polar-optical phonon-only mobilities; in the absence of impurity, it is quite apparent that these two processes govern low-T and room-T behavior, respectively.

It is interesting to note that the electron mobility in ETO is about 30% larger than in STO at room-T. This may appear inconsistent owing to their chemical and structural similarity, but in fact, the exchange of Sr with Eu produces a number of consequences, all favorable to the higher ETO mobility: first, the spatially broad Eu 5d orbitals overlap significantly with the Ti 3d orbitals, thus causing smaller effective masses than in STO. Additionally, the bigger Eu size results in sound velocity, deformation potential, ionic screening, and LO phonon frequencies which are all sensibly lower than the corresponding STO quantities. This establishes an advantage in the use of ETO for transport applications.

The analysis of the electronic properties suggests that thermoelectric transport of n-doped FM ETO should be strongly spin-dependent. It is worth emphasizing that the spin dependence does not stem from mobility, which is weakly sensitive to the magnetic order, but rather from the difference in majority and minority band occupancies. Indeed, we will see that band population is the key factor to obtain giant spin-dependence in thermopower. In the following sections, all the results are plot as a function of the carrier concentration across a range from $n = 1.6 \times 10^{15}$ to $n = 1.6 \times 10^{21}$ el per cm^3 (corresponding to 10^{-7}–10^{-1} el per f.u). For completeness, we show the results for three temperatures: 300 K, 100 K, and 10 K, albeit only the latter is close to T_c actually observed in n-doped ETO. In fact, the possibility of obtaining higher T_c cannot be excluded, *e.g.* in ETO-based superlattices or heterostructures, and thus they are worthy of consideration.

In Fig.6a, we report ε_F calculated with respect to the CBB (*i.e.* the bottom of Ti 3d majority bands) which in the figure is kept fixed at zero energy. The black curve is the spin splitting parameter $\Delta\varepsilon_{CBB}$ which here corresponds to the bottom of the minority Ti 3d bands. At low doping $\varepsilon_F \sim \ln(n/n_i)$, as for non-degenerate semiconductors, while $\Delta\varepsilon_{CBB}$ increases linearly with n as described in eqn (14). Since ε_F grows faster than $\Delta\varepsilon_{CBB}$, at any finite temperature a threshold value n_{th} exists for which ε_F overcomes the minority band bottom ($n_{th} = 1.6 \times 10^{20}$ cm^{-3}, 1.7×10^{20} cm^{-3}, 2.24×10^{20} cm^{-3} at 10 K, 100 K, and 300 K, respectively). Above n_{th} the minority bands start to become significantly populated, and then the spin dependence of transport and thermoelectric properties rapidly fade. In Fig. 6b we report the spin-polarized carrier fraction: at low doping this amounts to 88% at 300 K, 100% at 100 K and 10 K. At room T the spin polarization falls smoothly from its maximum value when n approaches n_{th}, while at 10 K the carriers remain fully spin-polarized up to n_{th}, and then at n_{th} the spin polarization drops abruptly.

Fig. 6c displays the conductivities of majority and minority carriers. They depend primarily on two ingredients (eqn (13)): the scattering rate $\tau^{\uparrow,\downarrow}$ and the effective charge which populates the respective bands. The latter is determined by the DOS overlap with the $\partial f/\partial\varepsilon$ bell, which can be described as a Gaussian function centered on $x = (\varepsilon^{\uparrow,\downarrow}_{CBB} - \varepsilon_F)/k_bT$. For majority carriers

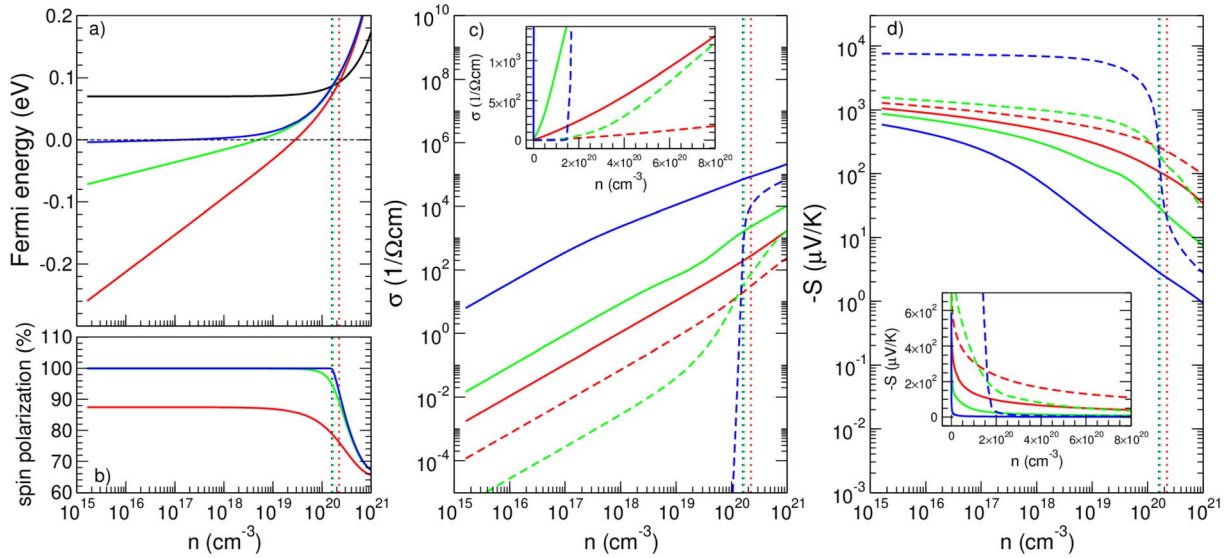

Fig. 6 Thermoelectric properties of n-doped FM ETO. Red, green, and blue lines refer to $T = 300$ K, 100 K, and 10 K, respectively. (a) Fermi energies; the CBB of majority conduction bands (dashed horizontal line) is fixed at zero energy. The black line indicates the spin-splitting of the conduction bands, *i.e.* the bottom of minority Ti 3d bands. Dotted vertical lines indicate the threshold n_{th} values for which the corresponding Fermi energy rises above the minority band bottom. (b) Fraction of spin polarized carriers, in percent, with respect to the total carrier density. (c) Spin-polarized conductivity; solid and dashed lines are conductivities of majority and minority channels, respectively. Inset: conductivities on a linear scale, showing the high-doping behavior. (d) Minus spin-polarized Seebeck coefficient for majority and minority channels. Inset: Seebeck coefficient on a linear scale.

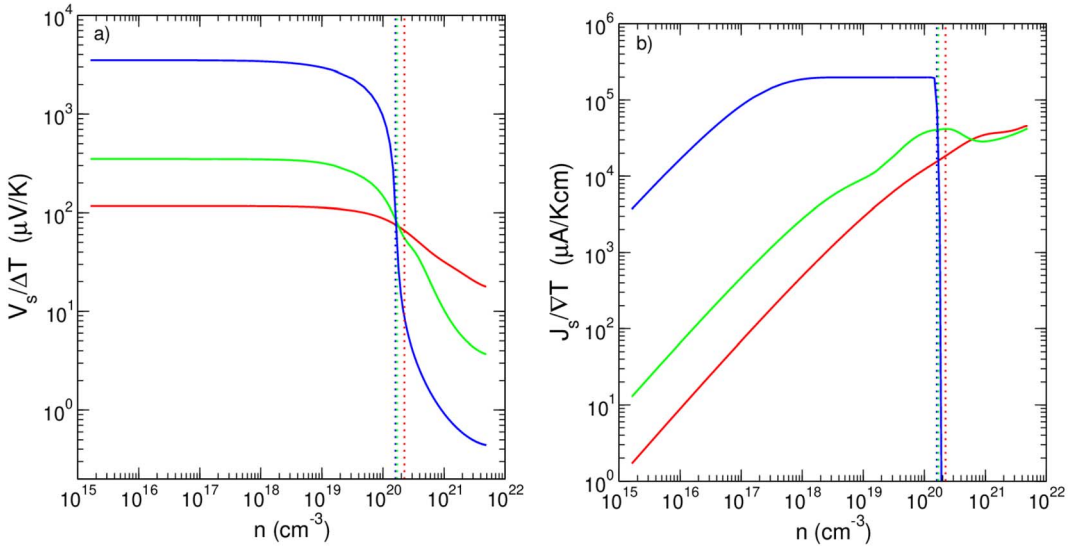

Fig. 7 (a) Spin voltage to temperature difference ratio; according to the definition of eqn (7), the positive value indicates that this is measured at the hotter side of the bar. (b) Spin current density (in μA cm^{-2} units) to temperature gradient (K cm^{-1}) ratio. Color code is the same as Fig. 6. The vertical dotted lines indicate n_{th}.

the scattering dependence dominates and $\sigma^{\uparrow}$ is essentially determined by $\tau^{\uparrow}$ (*i.e.* by the charge mobility); thus the largest $\sigma^{\uparrow}$ occurs at the lowest T. In contrast, for minority carriers, whose band edge is much farther from ε_F, the T dependence is primarily determined by the band population, *i.e.* by the exponential decay of the Gaussian function with x. At $T = 10$ K the minority band population (and in turn $\sigma^{\downarrow}$) is substantially null for $n < n_{th}$, and then it rises abruptly above the threshold. At low doping the relative $\sigma^{\uparrow}$ and $\sigma^{\downarrow}$ difference amounts to about an order of magnitude at 300 K, and four orders of magnitude at 10 K. For $n > n_{th}$ this difference decreases progressively, and we see that the decrease is faster at lower temperature, since at the low-temperature limit the spin-dependent effects fades more rapidly. In the high-doping regime, on the other hand, the mobility is substantially charge-independent (see Fig. 5), so the conductivities increase about linearly with n.

The same color code is used in Fig. 6d to plot $S^{\uparrow}$ and $S^{\downarrow}$; as expected for electrons they are negative at any charge concentration and temperature. The Seebeck trend with temperature of the two spin channels follows the inverse dependence on conductivity (eqn (13)) at any doping value. As previously discussed, the largest (in amplitude) Seebeck coefficient occurs for the less populated channel, whose band edge is much farther from ε_F. At low doping we obtain huge $S^{\downarrow}$ values: 1.3×10^3 μV K^{-1} at 300 K, 1.6×10^3 μV K^{-1} at 100 K, 7.5×10^3 μV K^{-1} at 10 K. As n approaches n_{th}, the Seebeck coefficient drops with a rate which is inverse to the absolute value: the larger the Seebeck, the faster the relative decrease.

For spin-caloritronic means, the most crucial aspect is the $S^{\uparrow}$ and $S^{\downarrow}$ difference, which is directly related to the spin voltage. In Fig. 7a we display the generated spin voltage per unitary T difference (eqn (8)). At any T, the voltage remains almost constant across a wide charge concentration interval, up to $n \sim 10^{19}$ cm^{-3}. In this range we obtain $V_s/\Delta T \sim 3$ mV at 10 K, 0.3 mV at 100 K, 0.1 mV at room T. We emphasize that these are giant values, when compared with other SSE observations reported in the literature; for example in NiFe FM films, values of nV/K order are estimated at room T;[1] in FM/NM heterostructures based on $Ni_{80}Fe_{20}$ permalloy, a spin voltage of 3.8 μV K^{-1} is reported;[2] in $Ga_{1-x}Mn_xAs$ thin films, values of μV K^{-1} are obtained at low T;[3] in more complicate ferromagnetic-oxide-silicon tunnel junctions, a voltage of 0.13 mV is generated.[6]

At low T the spin-polarization effects are larger but fade more rapidly with the increasing charge than at high T: for $T = 10$ K, V_s drops by four orders of magnitude when n comes across n_{th}. At room T, on the other hand, for n beyond n_{th}, V_s is only about an order of magnitude smaller than its low-doping counterpart, and it keeps a significant value even for charge densities as large as 10^{22} cm^{-3}.

In Fig. 7b we plot the spin current density per unit gradient (eqn (4)), *i.e.* the spin current density generated by a temperature difference of 1 K applied across a 1 cm-long sample. At low doping, the trend in temperature follows what is seen for $\sigma^{\uparrow}$: the spin current increases with n up to n_{th}, and then it sharply falls at 10 K, while it saturates at a maximum value at room T. We can see that for $T = 10$ K J_s remains nearly constant in the $n \sim 10^{18}$–10^{20} cm^{-3} doping range, reaching a giant value of 0.2 A cm^{-2} per unitary temperature gradient, whereas at room temperature the saturation value is 0.04 A cm^{-2} per unitary temperature gradient.

4. Conclusions

The occurrence of giant spin-polarized thermopower generated from temperature gradients opens fascinating perspectives in the design of materials for spin-caloritronic applications. In this work we presented a clear-cut prediction that giant SPSE can be obtained in n-doped ETO; in fact, this materials includes all the

favorable characteristics to the aim: (i) fairly mobile, and yet fully spin-polarized charge carriers, owing to a very peculiar coupling involving Eu 4f, Eu 5d, and Ti 3d orbitals; (ii) large charge tunability with the doping and/or field effect, as typical of oxide insulators; (iii) experimentally proved FM order at low temperature in a wide n-doping range; (iv) a Seebeck coefficient which is large in magnitude and, most of all, strongly spin-polarized. Our calculations show that at T_c it should be possible to observe spin voltages as large as a few mV K^{-1}, and spin current densities up to 0.2 A cm^{-2} per unitary temperature gradient, and that these values remain stable in a large interval of carrier density. These values rank among the highest presented in the literature for spin-caloritronic devices. Our analysis also furnishes conceptual guidelines and quantitative reference points for the optimization of the SPSE phenomenon in terms of carrier concentration and temperature. We have seen that the spin polarization effects progressively fade with increasing charge, and at any given temperature it is possible to define a threshold density, corresponding to the crossing point of the Fermi energy with the minority band bottom, above which the SPSE degrades. This decrease is very sharp at low temperature, and progressively smoother as temperature is increased. Finally, it is worth mentioning that ETO is epitaxially integrable in oxide heterostructures, where the control of device functionalities such as magnetic order and charge confinement can be more easily implemented. Albeit our calculations are for bulk ETO, it is reasonable to expect that our description of the SPSE could be significant even in the 2D limit.

Conflicts of interest

There are no conflicts of interest to declare.

Acknowledgements

Work supported by project PRIN 2017 “TOPSPIN”, funded by the Italian Ministry of University and Research (MIUR).

References

1 K. Uchida, S. Takahashi, K. Harii, J. Ieda, W. Koshibae, K. Ando, S. Maekawa and E. Saitoh, Observation of the spin Seebeck effect, *Nature*, 2008, **455**, 778–781.
2 A. Slachter, F. L. Bakker, J.-P. Adam and B. J. van Wees, Thermally driven spin injection from a ferromagnet into a non-magnetic metal, *Nat. Phys.*, 2010, **6**, 879–882.
3 C. M. Jaworski, J. Yang, S. Mack, D. D. Awschalom, J. P. Heremans and R. C. Myers, Observation of the spin-Seebeck effect in a ferromagnetic semiconductor, *Nat. Mater.*, 2010, **9**, 898–903.
4 C. M. Jaworski, J. Yang, S. Mack, D. D. Awschalom, R. C. Myers and J. P. Heremans, Spin-Seebeck Effect: A Phonon Driven Spin Distribution, *Phys. Rev. Lett.*, 2011, **106**, 186601.
5 K. Uchida, J. Xiao, H. Adachi, J. Ohe, S. Takahashi, J. Ieda, T. Ota, Y. Kajiwara, H. Umezawa, H. Kawai, G. E. W. Bauer, S. Maekawa and E. Saitoh, Spin Seebeck insulator, *Nat. Mater.*, 2010, **9**, 894–897.
6 J.-C. Le Breton, S. Sharma, H. Saito, S. Yuasa and R. Jansen, Thermal spin current from a ferromagnet to silicon by Seebeck spin tunnelling, *Nature*, 2011, **475**, 82–85.
7 J. Flipse, F. L. Bakker, A. Slachter, F. K. Dejene and B. J. vanWees, Direct observation of the spin-dependent Peltier effect, *Nat. Nanotechnol.*, 2012, **7**, 166–168.
8 F. K. Dejene, J. Flipse, G. E. W. Bauer and B. J. vanWees, Spin heat accumulation and spin-dependent temperatures in nanopillar spin valves, *Nat. Phys.*, 2013, **9**, 636–639.
9 C. M. Jaworski, R. C. Myers, E. Johnston-Halperin and J. P. Heremans, Giant spin Seebeck effect in a non-magnetic material, *Nature*, 2012, **487**, 2010–2012.
10 T. Kikkawa, D. Reitz, H. Ito, T. Makiuchi, T. Sugimoto, K. Tsunekawa, S. Daimon, K. Oyanagi, R. Ramos, S. Takahashi, Y. Shiomi, Y. Tserkovnyak and E. Saitoh, Observation of nuclear-spin Seebeck effect, *Nat. Commun.*, 2021, **12**, 4356.
11 H. Adachi, K. Uchida, E. Saitoh, J. Ohe, S. Takahashi and S. Maekawa, Gigantic enhancement of spin Seebeck effect by phonon drag, *Appl. Phys. Lett.*, 2010, **97**, 252506.
12 H. Adachi, J. Ohe, S. Takahashi and S. Maekawa, Linear-response theory of spin Seebeck effect in ferromagnetic insulators, *Phys. Rev. B*, 2022, **83**, 094410.
13 G. E. W. Bauer, E. Saitoh and B. J. van Wees, Spin caloritronics, *Nat. Mater.*, 2012, **11**, 391–399.
14 S. R. Boona, R. C. Myers and J. P. Heremans, Spin caloritronics, *Energy Environ. Sci.*, 2014, **7**, 885–910.
15 A. B. Cahaya, O. A. Tretiakov and G. E. W. Bauer, Spin Seebeck Power Conversion, *IEEE Trans. Magn.*, 2015, **51**, 0800414.
16 H. Yu, S. D. Brechet and J.-P. Ansermet, Spin caloritronics, origin and outlook, *Phys. Lett. A*, 2017, **381**, 825–837.
17 K. Uchida, Transport phenomena in spin caloritronics, *Proc. Jpn. Acad., Ser. B*, 2021, **97**, 69–88.
18 R. J. Elliott, Theory of the Effect of Spin-Orbit Coupling on Magnetic Resonance in Some Semiconductors, *Phys. Rev.*, 1954, **96**, 266–279.
19 Y. Yafet, g-factors and spin-lattice relaxation of conduction electrons, *Solid State Phys.*, 1963, **14**, 1–98.
20 Y. Yafet, Conduction electron spin relaxation in the superconducting state, *Phys. Lett. A*, 1983, **98**, 287–290.
21 P. Boross, B. Dora, A. Kiss and F. Simon, A unified theory of spin-relaxation due to spin-orbit coupling in metals and semiconductors, *Sci. Rep.*, 2012, **3**, 3233.
22 P. B. Allen, Boltzmann Theory and Resistivity of Metals, in *Quantum Theory of Real Materials*, ed. J. R. Chelikowsky and S. G. Louie, Kluwer, Boston, 1996, pp. 219–250.
23 G. Madsen and D. Singh, BoltzTraP. A Code for Calculating Band-Structure Dependent Quantities, *Comput. Phys. Commun.*, 2006, **175**, 67–71.
24 A. Filippetti, P. Delugas, M. J. Verstraete, I. Pallecchi, A. Gadaleta, D. Marré, D. F. Li, S. Gariglio and V. Fiorentini, Thermopower in Oxide Heterostructures: the Importance of Being Multiple-Band Conductors, *Phys. Rev. B: Condens. Matter Mater. Phys.*, 2012, **86**, 195301.

25 D. Puggioni, A. Filippetti and V. Fiorentini, Ordering and Multiple Phase Transitions in Ultra-Thin Nickelate Superlattices, *Phys. Rev. B: Condens. Matter Mater. Phys.*, 2012, **86**, 195132.

26 P. Delugas, A. Filippetti, M. Verstraete, I. Pallecchi, D. Marrè and V. Fiorentini, Doping-Induced Dimensional Crossover and Thermopower Burst in Nb-doped $SrTiO_3$ Superlattices, *Phys. Rev. B: Condens. Matter Mater. Phys.*, 2013, **88**, 045310.

27 P. Delugas, A. Filippetti, A. Gadaleta, I. Pallecchi, D. Marré and V. Fiorentini, Large Band Offset as Driving Force of 2-Dimensional Electron Confinement: the Case of $SrTiO_3$/$SrZrO_3$ interface, *Phys. Rev. B: Condens. Matter Mater. Phys.*, 2013, **88**, 115304.

28 P. Delugas, V. Fiorentini, A. Mattoni and A. Filippetti, Intrinsic Origin of the 2D Electron Gas at the (001) Surface of $SrTiO_3$, *Phys. Rev. B: Condens. Matter Mater. Phys.*, 2015, **91**, 115315.

29 A. Filippetti, A. Mattoni, C. Caddeo, M. I. Saba and P. Delugas, Low Electron-Polar Optical Phonon Scattering as a Fundamental Aspect of Carrier Mobility in Methylammonium Lead Halide $CH_3NH_3PbI_3$ Perovskites, *Phys. Chem. Chem. Phys.*, 2016, **18**, 15352–15362.

30 G. Kresse and J. Furthmüller, Efficient iterative schemes for *ab initio* total-energy calculations using a plane-wave basis set, *Phys. Rev. B: Condens. Matter Mater. Phys.*, 1996, **54**, 11169.

31 G. Kresse and D. Joubert, From ultrasoft pseudopotentials to the projector augmented-wave method, *Phys. Rev. B: Condens. Matter Mater. Phys.*, 1999, **59**, 1758.

32 J. P. Perdew, K. Burke and M. Ernzerhof, Generalized Gradient Approximation Made Simple, *Phys. Rev. Lett.*, 1996, **77**, 3865.

33 V. I. Anisimov, J. Zaanen and O. K. Andersen, Band theory and Mott insulators: Hubbard U instead of Stoner I, *Phys. Rev. B: Condens. Matter Mater. Phys.*, 1991, **44**, 943.

34 R. Shinde, S. S. R. K. C. Yamijala and B. M. Wong, Improved band gaps and structural properties from Wannier–Fermi–Löwdin self-interaction corrections for periodic systems, *J. Phys.: Condens. Matter*, 2021, **33**, 115501.

35 E. van Loef, U. Shirwadkar, L. S. Pandian, G. Ciampi, L. Stand, M.-H. Du, M. Koschan, M. Loyd, M. Zhuravleva, C. Melcher and K. Shah, Crystal growth, density functional theory, and scintillation properties of Tl_3LnCl_6:Ce^{3+} and $TlLn_2Cl_7$:Ce^{3+} (Ln = Y, Gd), *Nucl. Instrum. Methods Phys. Res.*, 2021, **995**, 165047.

36 R. Ranjan, H. S. Nabi and R. Pentcheva, Electronic structure and magnetism of $EuTiO_3$: a first-principles study, *J. Phys.: Condens. Matter*, 2007, **19**, 406217.

37 R. Di Capua, M. Verma, M. Radovic, N. C. Plumb, J. H. Dil, Z. Ristic, E. B. Guedes, G. M. De Luca, D. Preziosi, Z. Wang, A. P. Weber, R. Pentcheva and M. Salluzzo, Two-dimensional electron gas at the (001) surface of ferromagnetic $EuTiO_3$, *Phys. Rev. Res.*, 2021, **3**, L042038.

38 T. Katsufuji and H. Takagi, Coupling between magnetism and dielectric properties in quantum paraelectric $EuTiO_3$, *Phys. Rev. B: Condens. Matter Mater. Phys.*, 2001, **64**, 054415.

39 C. J. Fennie and K. M. Rabe, Magnetic and Electric Phase Control in Epitaxial $EuTiO_3$ from First Principles, *Phys. Rev. Lett.*, 2006, **97**, 267602.

40 J. H. Lee, L. Fang, E. Vlahos, X. Ke, Y. W. Jung, L. F. Kourkoutis, J.-W. Kim, P. J. Ryan, T. Heeg, M. Roeckerath, V. Goian, M. Bernhagen, R. Uecker, P. C. Hammel, K. M. Rabe, S. Kamba, J. Schubert, J. W. Freeland, D. A. Muller, C. J. Fennie, P. Schiffer, V. Gopalan, E. Johnston-Halperin and D. G. Schlom, A strong ferroelectric ferromagnet created by means of spin–lattice coupling, *Nature*, 2010, **466**, 954–958.

41 P. J. Ryan, J.-W. Kim, T. Birol, P. Thompson, J.-H. Lee, X. Ke, P. S. Normile, E. Karapetrova, P. Schiffer, S. D. Brown, C. J. Fennie and D. G. Schlom, Reversible control of magnetic interactions by electric field in a single-phase material, *Nat. Commun.*, 2013, **4**, 1334.

42 P. G. Reuvekamp, R. K. Kremer, J. Kohler and A. Bussmann-Holder, Spin-lattice coupling induced crossover from negative to positive magnetostriction in $EuTiO_3$, *Phys. Rev. B: Condens. Matter Mater. Phys.*, 2014, **90**, 094420.

43 P. Reuvekamp, K. Caslin, Z. Guguchia, H. Keller, R. K. Kremer, A. Simon, J. Köhler and A. Bussmann-Holder, Tiny cause with huge impact: polar instability through strong magneto-electric-elastic coupling in bulk $EuTiO_3$, *J. Phys.: Condens. Matter*, 2015, **27**, 262201.

44 Y. Lin, E.-M. Choi, P. Lu, X. Sun, R. Wu, C. Yun, B. Zhu, H. Wang, W. Li, T. Maity and J. MacManus-Driscoll, Vertical Strain-Driven Antiferromagnetic to Ferromagnetic Phase Transition in $EuTiO_3$ Nanocomposite Thin Films, *ACS Appl. Mater. Interfaces*, 2020, **12**, 8513–8521.

45 P. J. Ryan, G. E. Sterbinsky, Y. Choi, J. C. Woicik, L. Zhu, J. S. Jiang, J.-H. Lee, D. G. Schlom, T. Birol, S. D. Brown, P. B. J. Thompson, P. S. Normile, J. Lang and J.-W. Kim, Multiferroic behavior in $EuTiO_3$ films constrained by symmetry, *Phys. Rev. B*, 2020, **101**, 180409(R).

46 K. Fujita, N. Wakasugi, S. Murai, Y. Zong and K. Tanaka, High-quality antiferromagnetic $EuTiO_3$ epitaxial thin films on $SrTiO_3$ prepared by pulsed laser deposition and postannealing, *Appl. Phys. Lett.*, 2009, **94**, 062512.

47 J. H. Lee, X. Ke, N. J. Podraza, L. Fitting Kourkoutis, T. Heeg, M. Roeckerath, J. W. Freeland, C. J. Fennie, J. Schubert, D. A. Muller, P. Schiffer and D. G. Schlom, Optical band gap and magnetic properties of unstrained $EuTiO_3$ films, *Appl. Phys. Lett.*, 2009, **94**, 212509.

48 A. Bussmann-Holder and J. Köhler, Revisiting the fascinating properties of $EuTiO_3$ and its mixed crystals with $SrTiO_3$: Possible candidates for novel functionalities, *J. Phys. Chem. Solids*, 2015, **84**, 2–12.

49 A. Bussmann-Holder, K. Roleder, B. Stuhlhofer, G. Logvenov, I. Lazar, A. Soszyński, J. Koperski, A. Simon and J. Köhler, Transparent $EuTiO_3$ films: a possible two-dimensional magneto-optical Device, *Sci. Rep.*, 2016, **7**, 40621.

50 T. Katsufuji and Y. Tokura, Transport and magnetic properties of a ferromagnetic metal: $Eu_{1-x}R_xTiO_3$, *Phys. Rev. B: Condens. Matter Mater. Phys.*, 1999, **60**, R15021.

51 H. Akamatsu, Y. Kumagai, F. Oba, K. Fujita, H. Murakami, K. Tanaka and I. Tanaka, Antiferromagnetic superexchange

via 3d states of titanium in $EuTiO_3$ as seen from hybrid Hartree-Fock density functional calculations, *Phys. Rev. B: Condens. Matter Mater. Phys.*, 2011, **83**, 214421.

52 T. Kolodiazhnyi, M. Valant, J. R. Williams, M. Bugnet, G. A. Botton, N. Ohashi and Y. Sakka, Evidence of Eu^{2+} 4f electrons in the valence band spectra of $EuTiO_3$ and $EuZrO_3$, *J. Appl. Phys.*, 2012, **112**, 083719.

53 T. Birol and C. J. Fennie, Origin of giant spin-lattice coupling and the suppression of ferroelectricity in $EuTiO_3$ from first principles, *Phys. Rev. B: Condens. Matter Mater. Phys.*, 2013, **88**, 094103.

54 D. S. Ellis, H. Uchiyama, S. Tsutsui, K. Sugimoto, K. Kato, D. Ishikawa and A. Q. R. Baron, Phonon softening and dispersion in $EuTiO_3$, *Phys. Rev. B: Condens. Matter Mater. Phys.*, 2012, **86**, 220301.

55 V. Goian, S. Kamba, J. Hlinka, P. Vanek, A. A. Belik, T. Kolodiazhnyi and J. Petzelt, Polar phonon mixing in magnetoelectric $EuTiO_3$, *Eur. Phys. J. B*, 2009, **71**, 429–433.

56 S. Kamba, D. Nuzhnyy, P. Vanek, M. Savinov, K. Knizek, Z. Shen, E. Santava, K. Maca, M. Sadowski and J. Petzelt, Magnetodielectric effect and optic soft mode behaviour in quantum paraelectric $EuTiO_3$ ceramics, *Europhys. Lett.*, 2007, **80**, 27002.

57 S. Kamba, V. Goian, M. Orlita, D. Nuzhnyy, J. H. Lee, D. G. Schlom, K. Z. Rushchanskii, M. Lezaic, T. Birol, C. J. Fennie, P. Gemeiner, B. Dkhil, V. Bovtun, M. Kempa, J. Hlinka and J. Petzelt, Magnetodielectric effect and phonon properties of compressively strained $EuTiO_3$ thin films deposited on $(001)(LaAlO_3)_{0.29}$-$(SrAl_{1/2}Ta_{1/2}O_3)_{0.71}$, *Phys. Rev. B: Condens. Matter Mater. Phys.*, 2012, **85**, 094435.

58 Z. Gui and A. Janotti, Carrier-Density-Induced Ferromagnetism in $EuTiO_3$ Bulk and Heterostructures, *Phys. Rev. Lett.*, 2019, **123**, 127201.

59 L. Li, H. Zhou, J. Yan, D. Mandrus and V. Keppens, Research Update: Magnetic phase diagram of $EuTi_{1-x}B_xO_3$ (B = Zr, Nb), *APL Mater.*, 2014, **2**, 110701.

60 L. Li, J. R. Morris, M. R. Koehler, Z. Dun, H. Zhou, J. Yan, D. Mandrus and V. Keppens, Structural and magnetic phase transitions in $EuTi_{1-x}Nb_xO_3$, *Phys. Rev. B: Condens. Matter Mater. Phys.*, 2015, **92**, 024109.

61 T. Yamamoto, R. Yoshii, G. Bouilly, Y. Kobayashi, K. Fujita, Y. Kususe, Y. Matsushita, K. Tanaka and H. Kageyama, An Antiferro-to-Ferromagnetic Transition in $EuTiO_{3-x}H_x$ Induced by Hydride Substitution, *Inorg. Chem.*, 2015, **54**, 1501–1507.

62 G. M. De Luca, R. Di Capua, E. Di Gennaro, F. Miletto Granozio, D. Stornaiuolo and M. Salluzzo, Transport properties of a quasi-two-dimensional electron system formed in $LaAlO_3/EuTiO_3/SrTiO_3$ heterostructures, *Phys. Rev. B: Condens. Matter Mater. Phys.*, 2014, **89**, 224413.

63 D. Stornaiuolo, C. Cantoni, G. M. De Luca, R. Di Capua, E. Di Gennaro, G. Ghiringhelli, B. Jouault, D. Marrè, D. Massarotti, F. Miletto Granozio, I. Pallecchi, C. Piamonteze, S. Rusponi, F. Tafuri and M. Salluzzo, Tunable spin polarization and superconductivity in engineered oxide interfaces, *Nat. Mater.*, 2016, **15**, 278–284.

64 D. Stornaiuolo, B. Jouault, E. Di Gennaro, A. Sambri, M. D'Antuono, D. Massarotti, F. Miletto Granozio, R. Di Capua, G. M. De Luca, G. P. Pepe, F. Tafuri and M. Salluzzo, Interplay between spin-orbit coupling and ferromagnetism in magnetotransport properties of a spin-polarized oxide two-dimensional electron system, *Phys. Rev. B*, 2018, **98**, 075409.

65 R. Di Capua, M. Verma, M. Radovic, V. N. Strocov, C. Piamonteze, E. B. Guedes, N. C. Plumb, Y. Chen, M. D'Antuono, G. M. De Luca, E. Di Gennaro, D. Stornaiuolo, D. Preziosi, B. Jouault, F. Miletto Granozio, A. Sambri, R. Pentcheva, G. Ghiringhelli and M. Salluzzo, Orbital selective switching of ferromagnetism in an oxide quasi two-dimensional electron gas, *npj Quantum Mater.*, 2022, **7**, 41.

66 K. Ahadi, X. Lu, S. Salmani-Rezaie, P. B. Marshall, J. M. Rondinelli and S. Stemmer, Anisotropic magnetoresistance in the itinerant antiferromagnetic $EuTiO_3$, *Phys. Rev. B*, 2019, **99**, 041106(R).

67 K. Maruhashi, K. S. Takahashi, M. S. Bahramy, S. Shimizu, R. Kurihara, A. Miyake, M. Tokunaga, Y. Tokura and M. Kawasaki, Anisotropic Quantum Transport through a Single Spin Channel in the Magnetic Semiconductor $EuTiO_3$, *Adv. Mater.*, 2020, **32**, 1908315.

68 K. Ahadi, H. Kim and S. Stemmer, Spontaneous Hall effects in the electron system at the $SmTiO_3/EuTiO_3$ interface, *APL Mater.*, 2018, **6**, 056102.

69 K. S. Takahashi, M. Onoda, M. Kawasaki, N. Nagaosa and Y. Tokura, Control of the Anomalous Hall Effect by Doping in $Eu_{1-x}La_xTiO_3$ Thin Films, *Phys. Rev. Lett.*, 2009, **103**, 057204.

70 K. S. Takahashi, H. Ishizuka, T. Murata, Q. Y. Wang, Y. Tokura, N. Nagaosa and M. Kawasaki, Anomalous Hall effect derived from multiple Weyl nodes in high-mobility $EuTiO_3$ films, *Sci. Adv.*, 2018, **4**, eaar7880.

71 K. Rubi, P. Kumar, D. V. Maheswar Repaka, R. Chen, J.-S. Wang and R. Mahendiran, Giant magnetocaloric effect in magnetoelectric $Eu_{1-x}Ba_xTiO_3$, *Appl. Phys. Lett.*, 2014, **104**, 032407.

72 M. Allieta, M. Scavini, L. J. Spalek, V. Scagnoli, H. C. Walker, C. Panagopoulos, S. S. Saxena, T. Katsufuji and C. Mazzoli, Role of intrinsic disorder in the structural phase transition of magnetoelectric $EuTiO_3$, *Phys. Rev. B: Condens. Matter Mater. Phys.*, 2012, **85**, 184107.

73 K. Z. Rushchanskii, N. A. Spaldin and M. Lezaic, First-principles prediction of oxygen octahedral rotations in perovskite-structure $EuTiO_3$, *Phys. Rev. B: Condens. Matter Mater. Phys.*, 2012, **85**, 104109.

74 B. K. Ridley, *Quantum Processes in Semiconductors*, 2nd edn, Clarendon Press, Oxford, 1988.

75 B. K. Ridley, *J. Phys.: Condens. Matter*, 1998, **10**, 6717–6726.

76 D. R. Anderson, N. A. Zakhleniuk, M. Babiker, B. K. Ridley and C. R. Bennett, *Phys. Rev. B: Condens. Matter Mater. Phys.*, 2001, **63**, 245313.

